

A Multigrid Method for High Speed Reactive Flows

*Scott G. Sheffer**, *Antony Jameson†*, and *Luigi Martinelli‡*

CFD Laboratory for Engineering Analysis and Design
Department of Mechanical and Aerospace Engineering
Princeton University
Princeton, New Jersey 08544 U.S.A.

Abstract

This paper presents a multigrid method for computing inviscid and viscous high speed steady-state hydrogen/oxygen and hydrogen/air reactive flows. The governing equations for reactive flow are solved using an explicit multigrid algorithm while treating the chemical source terms in a point implicit manner. The CUSP (Convective Upwind and Split Pressure) scheme is used to provide necessary artificial dissipation without contaminating the solution. Results indicate good multigrid speedups and adequate resolution of the reaction zone in both inviscid axisymmetric and viscous two-dimensional test cases. The method lends itself to efficient parallel computations, thus enabling the calculation of reactive flows with detailed chemical kinetics.

Nomenclature

$C(w_{ij})$	convective Euler fluxes
$D(w_{ij})$	diffusive and dissipative fluxes
E	total energy (internal, chemical and kinetic)
\mathbf{f}, \mathbf{g}	Euler flux vectors
\mathbf{fv}, \mathbf{gv}	diffusive flux vectors
h_i	static enthalpy of species i
M	Mach number
p	static pressure
\mathbf{q}	conductive heat flux vector
R	mixture gas constant
$R(w_{ij})$	total flux residual for cell i,j
T	static temperature
u, v	Cartesian velocity components
u_{di}, v_{di}	diffusion velocity components for species i
V_{ij}	volume of cell i,j
\mathbf{w}	vector of flow variables
γ	mixture ratio of specific heats

Copyright ©1997 by the Authors. Published by the AIAA Inc. with permission.

* Graduate Student, Student Member AIAA

†James S. McDonnell Distinguished University Professor of Aerospace Engineering, AIAA Fellow

‡Assistant Professor of Aerospace Engineering, AIAA Member

ρ	density
ρ_i	density of species i
τ	viscous stress
ω	chemical source term
$\Omega, \partial\Omega$	cell element and boundary

Introduction

The simulation of high speed chemically reacting flows is a very challenging area for computational efforts. The presence of shock waves necessitates good shock capturing properties, while chemical reactions require avoiding excessive numerical dissipation so that the solution remains uncontaminated. Viscous effects, heat conduction and species diffusion complicate reactive flow calculations, both from the increased computational work required and because of possible interactions between the chemistry and these effects. Diffusion of radical species in a boundary layer may significantly alter the resulting flowfield. Exponential increases and decreases of radical species in small spatial zones near shocks lead to large gradients that must simultaneously be captured without oscillation and without unnecessary dissipation. In addition, the stiff nature of the chemical source terms makes the integration of the governing equations very difficult and time consuming.

The inherent inaccuracy of chemical rate data presents another challenge to modeling reactive flows. The turn around time of reactive flow simulations must be made short enough so that varying rate coefficients may be examined to determine which set is the most appropriate for modeling a particular phenomena.

The use of multigrid acceleration for reactive flow calculations has not been adequately examined. Bussing and Murman [1] explored the use of multigrid, but only for their one-dimensional calculations. Multigrid techniques may have been thought to be too dissipative and cause radical species to be moved

to physically incorrect regions. However, proper multigrid techniques, in which the coarse grids are forced by the fine grid solution, can in fact be used to compute chemically reacting flows. With the addition of viscous effects and species diffusion, a way to accelerate convergence is sorely needed. While parallelization will decrease the computational time associated with a numerical simulation, multigrid techniques represent an untapped potential for convergence acceleration of reactive flow calculations.

Because most chemical reactions have characteristic times much less than those of the convective flow field, explicit schemes are handicapped in computing such flows. The time step for an explicit scheme is proportional to the shortest characteristic time, so that stability restrictions require very short time steps in reactive flow simulations. This short time step leads to very long simulation times for steady state computations.

Several ways to overcome this limitation of explicit schemes have been explored. The first is to use a fully implicit scheme for the steady state computation, thus removing stability limitations completely. Another way of reducing the effect of the chemical term stiffness is to treat the source term in a point implicit manner. In this formulation due to Bussing and Murman [1], the source term at the next time level is linearized about the current time level, leading to a fully explicit equation at the cost of a matrix inversion. This action has the effect of preconditioning the species continuity equations, rescaling the chemical characteristic time so that it is of the same order as the convective characteristic time.

In this work, the point-implicit formulation of Bussing and Murman is combined with an explicit multi-grid solver [11] using CUSP dissipation to compute high speed reactive flows. The fully explicit algorithm is parallelized using the MPI standard on an IBM SP-2 to achieve high parallel speedups.

Governing Equations

The two-dimensional equations for chemically reacting flow can be written in a Cartesian coordinate system (x, y) as:

$$\frac{\partial \mathbf{w}}{\partial t} + \frac{\partial(\mathbf{f} - \mathbf{f}_v)}{\partial x} + \frac{\partial(\mathbf{g} - \mathbf{g}_v)}{\partial y} = \dot{\omega}, \quad (1)$$

where \mathbf{w} is the vector of flow variables, \mathbf{f} and \mathbf{g} are the convective flux vectors, \mathbf{f}_v and \mathbf{g}_v are the diffusive flux vectors and $\dot{\omega}$ is the vector of source terms. Consider a control volume Ω with boundary $\partial\Omega$. The equations of motion of the fluid can then

be written in integral form as

$$\begin{aligned} \frac{d}{dt} \iint_{\Omega} \mathbf{w} \, dx \, dy + \oint_{\partial\Omega} (\mathbf{f} \, dy - \mathbf{g} \, dx) = \\ \oint_{\partial\Omega} (\mathbf{f}_v \, dy - \mathbf{g}_v \, dx) + \iint_{\Omega} \dot{\omega} \, dx \, dy, \end{aligned} \quad (2)$$

where \mathbf{w} is the vector of flow variables

$$\mathbf{w} = \begin{Bmatrix} \rho_i \\ \rho u \\ \rho v \\ \rho E \end{Bmatrix},$$

\mathbf{f} , \mathbf{g} are the Euler flux vectors

$$\mathbf{f} = \begin{Bmatrix} \rho_i u \\ \rho u^2 + p \\ \rho u v \\ \rho E u + p u \end{Bmatrix}, \quad \mathbf{g} = \begin{Bmatrix} \rho_i v \\ \rho u v \\ \rho v^2 + p \\ \rho E v + p v \end{Bmatrix},$$

\mathbf{f}_v , \mathbf{g}_v are the diffusive flux vectors including species diffusion effects

$$\begin{aligned} \mathbf{f}_v = & \begin{Bmatrix} -\rho_i u_{di} \\ \tau_{xx} \\ \tau_{xy} \\ -q_x - \sum_{i=1}^N \rho_i u_{di} h_i + \tau_{xx} u + \tau_{xy} v \end{Bmatrix}, \\ \mathbf{g}_v = & \begin{Bmatrix} -\rho_i v_{di} \\ \tau_{yx} \\ \tau_{yy} \\ -q_y - \sum_{i=1}^N \rho_i v_{di} h_i + \tau_{yx} u + \tau_{yy} v \end{Bmatrix}, \end{aligned}$$

and $\dot{\omega}$ is the chemical source vector

$$\dot{\omega} = \begin{Bmatrix} \dot{\omega}_i \\ 0 \\ 0 \\ 0 \end{Bmatrix}.$$

In these equations, $i = 1, \dots, N$ and N is the number of species. For a thermally perfect gas, pressure may be determined from

$$p = \rho R T$$

where R is the mixture gas constant. The density is found from

$$\rho = \sum_{i=1}^N \rho_i$$

Temperature may be determined from the following relation,

$$E = e + \frac{1}{2} (u^2 + v^2) = \sum_{i=1}^N \frac{\rho_i}{\rho} h_i - \frac{p}{\rho} + \frac{1}{2} (u^2 + v^2)$$

where h_i are the individual species enthalpies which depend solely on temperature for a thermally perfect gas.

Chemical Model

One strength of the current work is that the resulting code can use an arbitrary chemical model, thus allowing for quick comparison of reaction sets. Therefore, several different chemistry models for hydrogen-air combustion are used in this paper. The first is a reduced equation model for hydrogen-air combustion due to Evans and Schexnayder [3] involving seven species and eight reactions. Nitrogen in this set is treated as an inert diluent. The second group of rate equations is the nine species, nineteen reaction modified model of Jachimowski [5] and Wilson and MacCormack [19]. Again, nitrogen is treated as an inert diluent because reactions involving nitrogen have been determined to be negligible below Mach 5 [13]. Another chemistry model is that of Yetter *et al.* [22, 9, 21]. This mechanism, which is part of a broader mechanism for the CO/H₂O/O₂ system, contains eight reacting species and 21 reactions. The last model was one proposed by Westbrook [18] which includes eight reacting species and seventeen reactions for hydrogen-oxygen combustion.

Numerical Model

Flow Equations

The governing equations are solved using a conservative second-order accurate finite volume formulation in which the chemical source terms are treated point implicitly.

When the integral governing equations 2 are independently applied to each cell i, j in the domain, we obtain a set of coupled ordinary differential equations of the form

$$\frac{d}{dt}(\mathbf{w}_{ij})V_{ij} + \mathbf{C}(\mathbf{w}_{ij}) + \mathbf{D}(\mathbf{w}_{ij}) = \dot{\omega}V_{ij}, \quad (3)$$

where $\mathbf{C}(\mathbf{w}_{ij})$ are the convective Euler fluxes, $\mathbf{D}(\mathbf{w}_{ij})$ includes the diffusive fluxes and the artificial dissipation fluxes added for numerical stability reasons and $\dot{\omega}V_{ij}$ are the chemical source terms. This equation (3) can be rewritten as follows (drop the i, j subscripts for clarity):

$$\frac{d}{dt}[\mathbf{w}]V + \mathbf{R}(\mathbf{w}) = \dot{\omega}V, \quad (4)$$

where \mathbf{R} is the sum of the two flux contributions. The governing ordinary differential equations are solved using a standard five-stage time stepping scheme [12].

Chemical Source Terms

The chemical source vector $\dot{\omega}$ was treated in a point implicit manner [1]. An explicit treatment of the

source terms leads, in general, to a time step restriction due to the stability limitation of the explicit scheme. This time step can be orders of magnitude less than the time step of the convective terms. Treating the source terms implicitly removes the stability criterion at the expense of a matrix inversion. The point implicit treatment has the result of reducing the stiffness of the problem by effectively rescaling the characteristic time of the reactions so that their magnitudes are commensurate with the convective characteristic time.

This treatment necessitates the inversion of the source term Jacobian matrix with dimension $N \times N$ where N is the number of species present in the flow. An inversion for the momentum and energy equations is not necessary due to the absence of chemical source terms in those equations. This $N \times N$ inversion is done only during the first stage of each time step of the solver and is retained and used for the succeeding four stages. This time-saving step has no effect on the results of the computation.

Because the chemical source terms have been treated implicitly, the time step limitation of the explicit time integration scheme depends solely on the spectral radius of the flux Jacobian.

Numerical Dissipation

The Convective Upwind and Split Pressure (CUSP) scheme provides excellent resolution of shocks at high Mach numbers at a reasonable computational cost [6, 7]. The CUSP splitting is combined with a LED or ELED limiter to achieve second order accuracy in smooth regions with oscillation-free capture of shocks and large gradient regions. CUSP has been shown to be an accurate and effective dissipation scheme for viscous flows [17] and high speed reactive flows [15, 14].

Boundary Conditions

The surface boundary is modeled as an adiabatic, non-catalytic inert surface. For Euler calculations, flow tangency is enforced at the the surface while a no-slip boundary condition is used for viscous flows. Due to the supersonic nature of the flow, outflow boundary quantities are extrapolated from the interior and inflow quantities are taken to be free stream values.

Free stream values of radical species are set to a mass fraction of 1×10^{-12} . Varying this value did not affect the results.

Parallelization

The MPI standard is used to parallelize the code on an IBM SP-2. A static domain decomposition with two-level halos for flow quantities and one-level halos for grid information is used. The current point implicit scheme will achieve a higher level of speedup as compared to a convective flow code alone due to the larger number of operations that take place per cell [14].

Multigrid Convergence Acceleration

Multigrid acceleration has been applied quite successfully to the solution of both the non-reactive Euler and Navier-Stokes equations [11, 12, 17]. However, the application of multigrid methods to reactive flow calculations has been limited. Bussing and Murman [1] reported success in using Ni's multigrid method for one-dimensional reactive flow calculations. Additional examples of multigrid acceleration for reactive flows are lacking.

The approach taken in this paper is to use a previously validated multigrid solver [11, 12, 17] and include chemical source terms on all levels [14]. The coarse grid corrections to the species densities are limited to ensure that no mass fraction becomes negative. Varying degrees of underrelaxation can be used to enhance the convergence rate while capturing the sharp gradients and large radical growth regions that characterize reactive flow problems.

Results and Discussion

The formulation described in this paper was applied to both inviscid axisymmetric flows over spherical blunt bodies and two-dimensional viscous ramp flows.

Stoichiometric hydrogen/oxygen flow over an axisymmetric spherical tip projectile at $M = 3.55$ was simulated using the reduced chemistry model (six species, eight reactions) of Evans and Schexnayder [3]. This corresponds to an experiment conducted by Lehr [10] which is shown in Figure 1. The diameter of this projectile is 15 mm. The free stream temperature is 292 K and the free stream pressure is 24800 Pa. The grid in this case is 64×64 cells. The bow shock in front of the body raises the temperature of the flow so that, after an induction zone, the flow reacts. As shown in Figure 2, the length of the induction zone varies depending on the post shock temperature which corresponds to the relative strength of the shock. Temperature is approximately constant in the induction zone as radicals

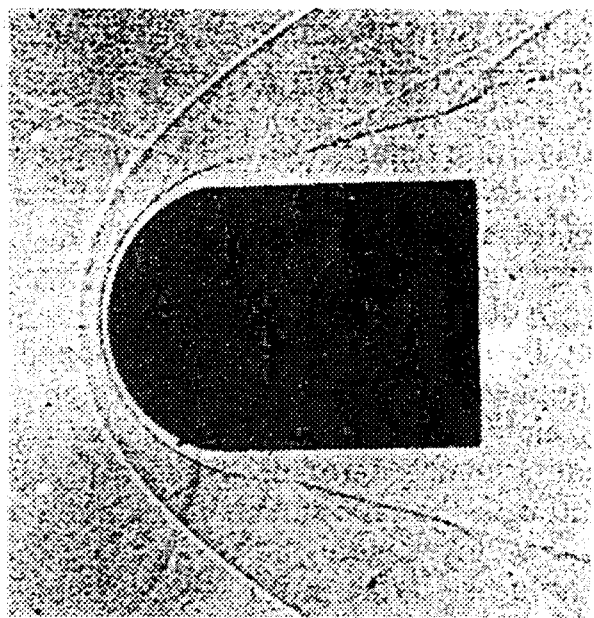


Figure 1: Experimental shockwave and reaction front: $M = 3.55$ hydrogen/oxygen, from Lehr [10].

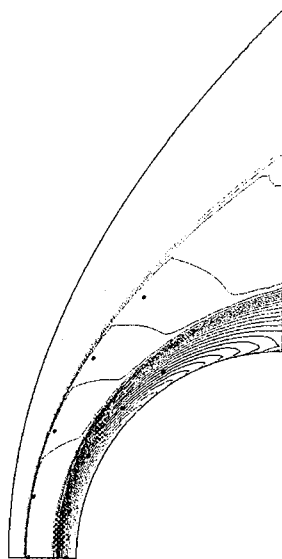


Figure 2: Temperature contours: $M = 3.55$ hydrogen/oxygen. Contour levels in K: min: 250, max: 3130, inc: 93. Grid size: 64×64 . Circles indicate experimental shock and heat release locations.

build up to the necessary levels to react and produce water vapor. The production of water vapor is accompanied by heat release which raises the temperature and, because pressure is nearly constant across the reaction zone, lowers the density. Figure 3 shows the temperature along the stagnation streamline computed using the Evans and Schexnayder reaction model and also the Jachimowski eight species, nineteen reaction modified model. The eight

for the chemistry, since it produced a shock location that was closer to the body on the 64×64 grid. Temperature contours for this finer grid simulation are presented in Figure 4 along with experimental shock and heat release front locations. As can be seen, the agreement between the experimental results and the numerical simulation is much better on this finer grid. The increased resolution has moved the shock closer to the body, increased the length of the induction zone and moved the heat release front closer to the body. Density and pressure contours are presented in Figures 5 and 6.

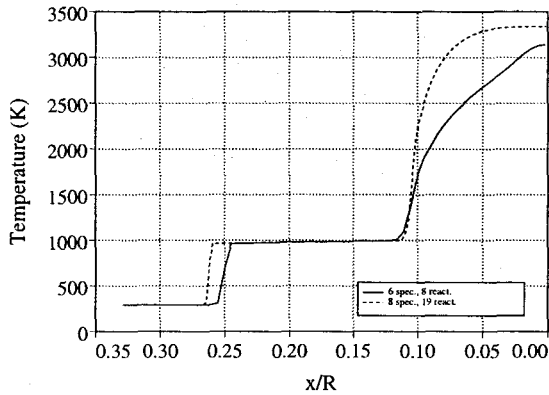


Figure 3: Temperature along stagnation streamline for two different chemical models: $M = 3.55$ hydrogen/oxygen; projectile surface at $x/R = 0.00$. Grid size: 64×64 .

species, nineteen reaction model produced a slightly different shock location, while the point of heat release is close to the Evans and Schexnayder model. The only difference between these two calculations was the chemistry model used: both models used the same algorithm and grid and were converged to the same level of accuracy. Thus, even though both simulations are converged, different solutions result because the mathematical models were slightly different in the modeling of the chemistry. The difference in shock location could be explained by a difference in relaxation characteristics behind the shock due to the chemical models. In addition, the heat release profiles lead to slightly different static pressures behind the heat release region, which could result in different shock positions. Figure 3 indicates that the numerical dissipation scheme is providing the necessary dissipation in regions of steep gradients, such as the shock, to prevent oscillations and preserve monotonicity while still allowing sharp resolution.

However, upon examining Figure 2, one may notice that the numerical solution differs slightly from the experimental shock location and heat release front. Thus, another simulation was performed on a 64×128 cell grid which had twice the number of grid cells in the normal direction as the 64×64 grid had. The Evans and Schexnayder model was used

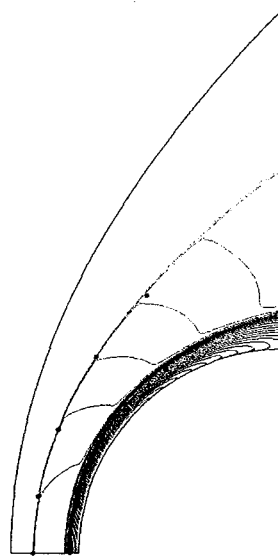


Figure 4: Temperature contours: $M = 3.55$ hydrogen/oxygen. Contour levels in K: min: 250, max: 3130, inc: 93. Grid size: 64×128 . Circles indicate experimental shock and heat release locations.

The temperature along the stagnation streamline for the 64×128 grid is shown in Figure 7. As in the case of the 64×64 cell grid, the flow passes through a shock which is followed by an induction zone where radicals are created due to the higher temperature. After sufficient amounts of radicals have been formed, water vapor is created, increasing the temperature and further hastening the reaction.

The mass fractions of the reactants and products for the Evans model simulation on the 64×128 grid are plotted in Figure 8. As expected, the reactants have almost constant mass fraction through the shock and only begin to be consumed in the heat release region. Water vapor is not formed in any appreciable quantity until the heat release region. It should also be noted that the mass fraction profiles are monotonic; no overshoots in the mass fraction of these primary components is observed, again indicating good performance of the CUSP dissipation scheme.

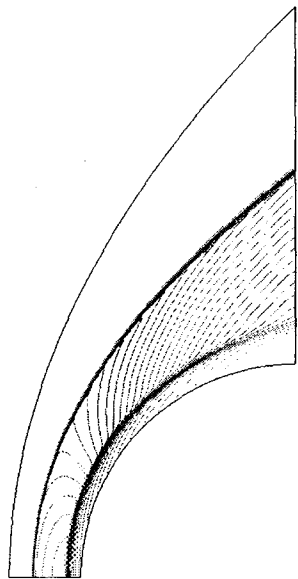


Figure 5: Density contours: $M = 3.55$ hydrogen/oxygen. Contour levels in kg/m^3 : min: 0.05, max: 0.6, inc: 0.016. Grid size: 64×128 .

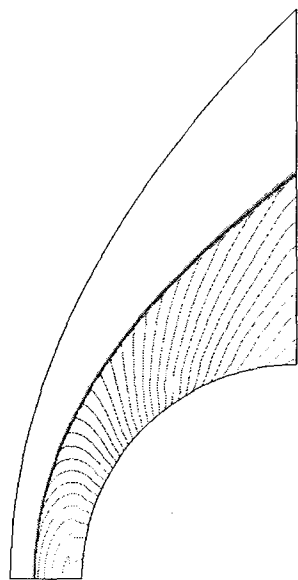


Figure 6: Normalized pressure contours: $M = 3.55$ hydrogen/oxygen. Contour levels (p/p_∞): min: 1.0, max: 16.5, inc: 0.5. Grid size: 64×128 .

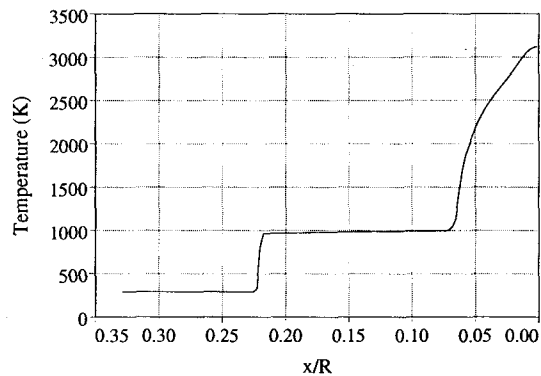


Figure 7: Temperature along stagnation streamline: $M = 3.55$ hydrogen/oxygen; projectile surface at $x/R = 0.00$. Grid size: 64×128 .

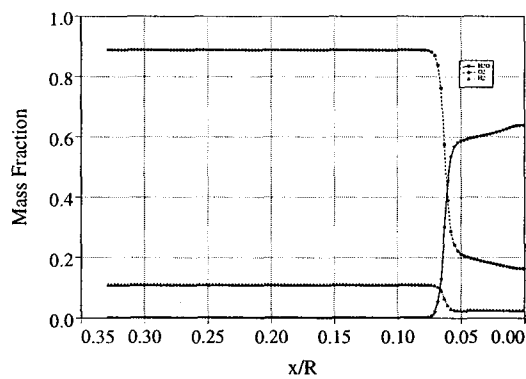


Figure 8: Mass fractions along stagnation streamline: $M = 3.55$ hydrogen/oxygen. Shock location is at $x/R = 0.22$; heat release region begins at $x/R = 0.065$; projectile surface at $x/R = 0.00$. Grid size: 64×128 .

The growth and destruction of radical species is depicted in Figure 9 for the Evans model. This figure

problem without compromising the accuracy of the solution.

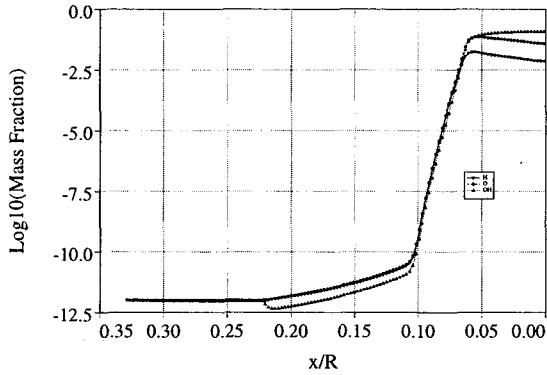


Figure 9: Logarithm of radical mass fractions along stagnation streamline: $M = 3.55$ hydrogen/oxygen. Shock location is at $x/R = 0.22$; heat release region begins at $x/R = 0.065$; projectile surface at $x/R = 0.00$. Grid size: 64×128 .

shows the logarithm of the mass fractions of the radical species. Exponential growth can be observed in the induction zone, which is to be expected. After a small region of slow growth, the radical mass fractions grow approximately nine orders of magnitude in a very short distance, which is a testament to the ability of the CUSP splitting and the flux limiter to capture large changes in the conservative variables without oscillation and without undue damping. The mass fraction of the radicals does not decrease greatly after the heat release zone, even with the formation of a great deal of water vapor. This is due to the conversion of the reactants into radical species which then combine directly to form water.

Upon examination of Figure 4, it can be seen that the agreement between the computation and experiment is quite good. This computation also agrees favorably with the simulation of Yungster *et al.* [23] who limited the cell Damköhler number so that the heat release was spread out among two to three cells. No such limitation is necessary using the current formulation.

Figures 10 and 11 show the convergence histories for the six species, eight reaction 64×64 cell calculation without and with multigrid acceleration. The convergence histories present the root mean squared residual of the density of water and the number of supersonic cells in the domain versus the number of cycles. The initial increase in the density residual is due to the production of water as the flow initially reacts and the bow shock and reaction zone move outward from the body. The use of multigrid provides a significant convergence acceleration in this

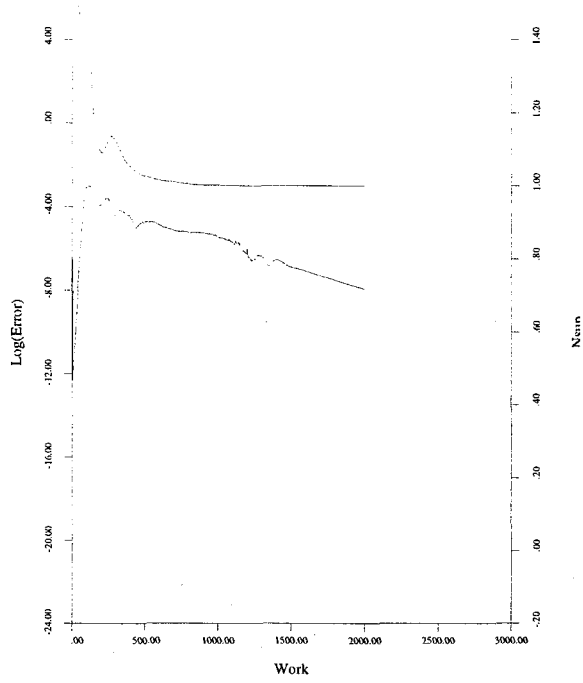


Figure 10: Single grid convergence history: $M = 3.55$ hydrogen/oxygen. Grid size: 64×64 .

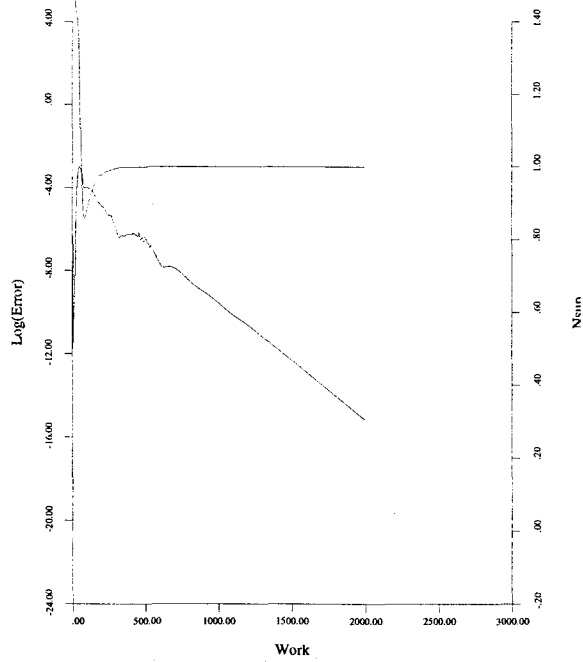


Figure 11: Multigrid convergence history: $M = 3.55$ hydrogen/oxygen. Grid size: 64×64 .

The single grid calculation converged about six orders of magnitude in 2000 iterations, consuming 995 seconds (wall clock) using four processors of an IBM

SP-2. The multigrid calculation, using only two levels of multigrid for this 64×64 mesh, converged fourteen orders of magnitude in 2000 iterations while requiring 1250 seconds on four processors. The same level of convergence (which results in a solution that does not change) as the single grid case using multigrid takes about 800 iterations at a cost of 500 seconds, almost halving the computational time. The converged solutions with and without multigrid acceleration are virtually identical due to the correct forcing of the coarse grid by the fine grid solution. No unphysical diffusion of radical species is seen. The convergence history for the multigrid 64×128 cell simulation is shown in Figure 12. Multigrid again provides a significant convergence acceleration.

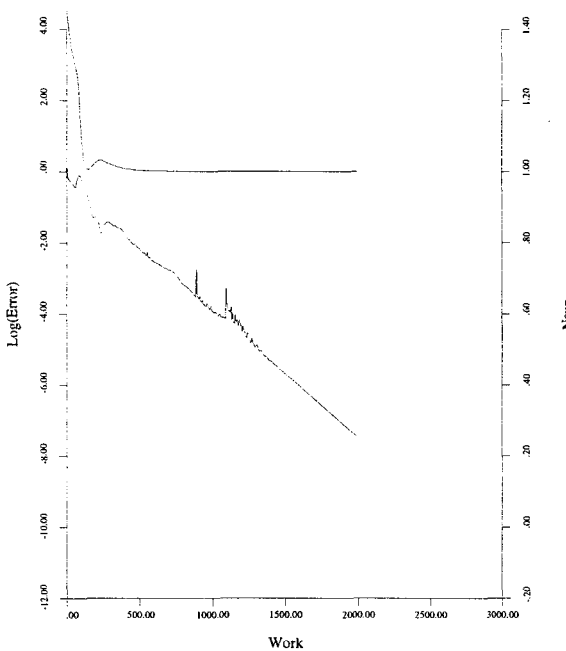


Figure 12: Multigrid convergence history: $M = 3.55$ hydrogen/oxygen. Grid size: 64×128 .

A two dimensional viscous reactive test case was taken from an experiment performed by Fielding [4]. In this experiment (Figure 13), a wedge of half angle 6.34° was placed in a free stream of partially reacted hydrogen and air. The free stream Mach number was 2.10, the free stream temperature was approximately 569 K and the pressure was 0.060 atmospheres. The object of the experiment was to see if radical-seeded hydrogen-air mixtures would react at low pressures over a wedge after passing through an oblique shock. The mass fractions of the inlet flow were determined by Fielding using a one dimensional reacting gas code and are given in Table 1. Hydrogen had been injected into the air stream upstream of the ramp, partially reacted and then expanded so that the flow constituents became

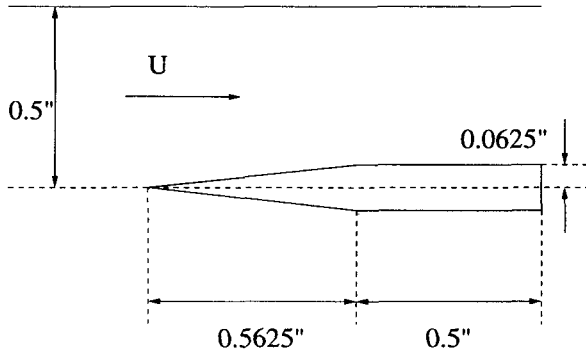


Figure 13: Experimental setup for $M = 2.10$ viscous wedge.

Species	Mass Fraction
H_2	6.86×10^{-3}
O_2	1.75×10^{-1}
H_2O	2.86×10^{-2}
N_2	7.84×10^{-1}
H	2.33×10^{-4}
O	9.66×10^{-4}
OH	1.65×10^{-4}
HO_2	3.97×10^{-3}
H_2O_2	4.76×10^{-10}

Table 1: Free stream mass fractions for $M = 2.10$ hydrogen-air viscous wedge flow.

frozen. It was assumed that nitrogen was an inert diluent. Due to the low pressure, the Reynolds number at the end of the ramp is approximately 33000 so that fully laminar flow may be assumed. Species diffusion and heat conduction effects are included in the simulation. The nine species, 21 reaction model of Yetter *et al.* was used because it had been the model utilized to generate the composition of the incoming flow.

The flow was simulated on a grid with 128 cells in the streamwise direction and 96 in the direction normal to the plate. Symmetry boundary conditions were implemented along the centerline of the flow upstream of the wedge so that the governing equations were solved on only half of the experimental domain. The grid was clustered near the leading edge of the wedge to properly resolve the growth of the boundary layer and the shock attachment. Cells were also clustered near the ramp to resolve the boundary layer structure adequately; approximately 32 cells were within the boundary layer.

Figure 14 presents contours of density for this flow. The relatively thick boundary layer is immediately noticeable. Because of this thick boundary layer, the shock near the leading edge of the plate is at a much higher angle than the region away from the

ramp. The growing displacement thickness from the boundary layer causes the main flow to see an effectively curved wall and thus, weak expansion waves are formed to adjust the curvature of the shock. It is also important to point out the absence of large heat release regions even though the domain near the leading edge experiences a relatively large compression. The shock angle obtained from the numerical simulation is 35.0° while the experimental shock angle is 34.5° .

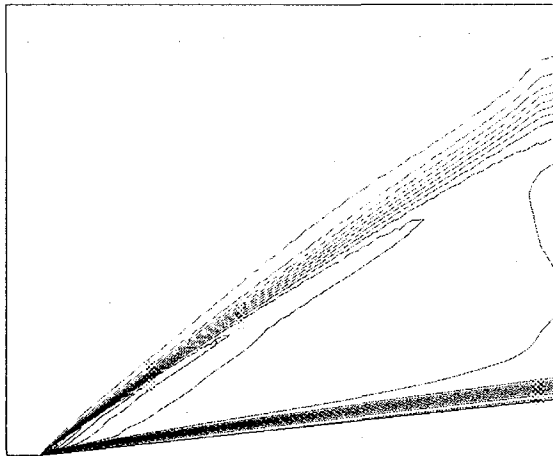


Figure 14: Density contours: $M = 2.10$ hydrogen/air 6.34° viscous ramp. Contour levels in kg/m^3 : min: 0.033, max: 0.056, inc: 0.00129.

The pressure field (Figure 15) yields trends similar to the density field. There is curvature of the shock near the leading edge and expansion waves may be seen in the region behind the oblique shock. Very little change in the pressure is seen through the boundary layer.

The lack of progress of the reaction may be understood by viewing Figure 16, which shows contours of the logarithm of OH mass fraction. It is immediately obvious that the inlet mass fractions are not in an equilibrium state, as rapid reaction takes place in the free stream flow, producing more OH. Behind the shock, the increased pressure and temperature and slightly increased residence time cause faster formation of OH, but the post shock temperature and pressures are not sufficient to allow large quantities of OH to strip hydrogen atoms from H_2 molecules and form water vapor. Near the ramp surface, it can be observed that some OH is being consumed and transformed to water. This is due to the higher temperature in the boundary layer near the wall, and because the molecules in that region have a longer residence time at those higher temperatures due to the lower velocity near the wall. The maximum water mass fraction is approximately 3%, which is not much greater than the free stream water mass frac-

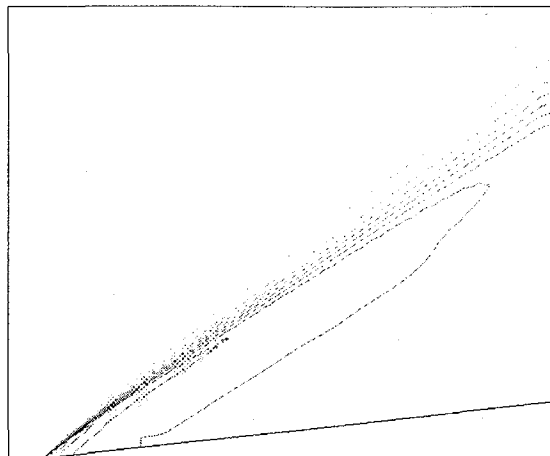


Figure 15: Normalized pressure contours: $M = 2.10$ hydrogen/air 6.34° viscous ramp. Contour levels (p/p_∞): min: 1.0, max: 3.06, inc: 0.0857.

tion from Table 1. This small amount of water production and heat release is not sufficient to cause thermal runaway, greater reaction and greater heat release. These results agree qualitatively with the

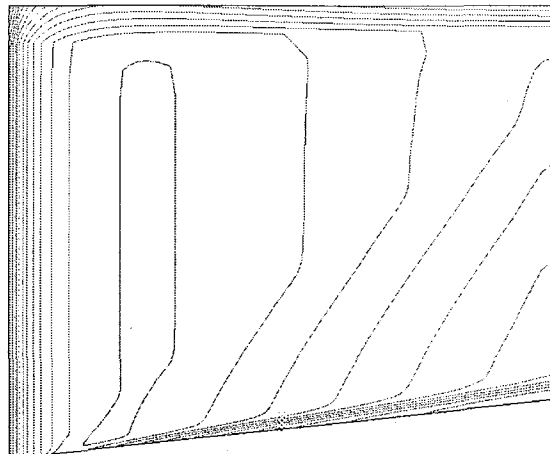


Figure 16: Logarithm of OH mass fraction contours: $M = 2.10$ hydrogen/air 6.34° viscous ramp. Contour levels: min: -3.33, max: -2.65, inc: 0.057.

experimental findings. Excited OH fluorescence was observed in the region behind the shock and near the leading edge, but large regions of heat release were absent.

Figures 17 and 18 show convergence histories for this calculation without and with multigrid acceleration. The single grid calculation converged approximately three orders of magnitude in 2000 iterations. The computational cost of this calculation was 4578 seconds using six processors of an IBM SP-2. The multigrid calculation with two levels of grids converged six orders of magnitude after 2000 iterations

in 7992 seconds of wall clock time. The multigrid calculation achieved the same convergence level as the single grid calculation in approximately 2550 seconds, which is 1.80 times faster than the single grid calculation. The results of both simulations are virtually identical. As in the inviscid case presented previously, no unphysical diffusion of species is seen due to the correct forcing of the coarse grid.

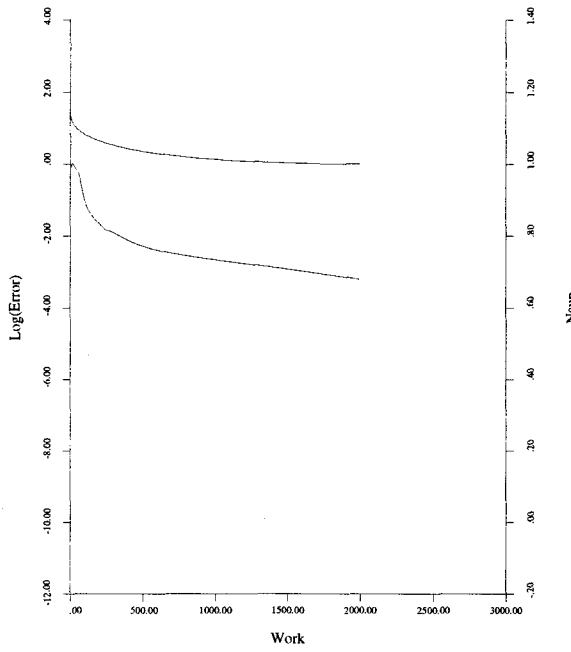


Figure 17: Single grid convergence history: $M = 2.10$ hydrogen/air 6.34° viscous ramp. Grid size: 128×96 .

The third test case consisted of a stoichiometric hydrogen/air flow over a 10° viscous ramp. The freestream Mach number was 4.0, the freestream temperature was 1200 K and the freestream pressure was one atmosphere. The 2 cm ramp was preceded by a 1 cm solid wall section. The effects of viscosity, heat conduction and species diffusion are all included in this computation. This is a common viscous/reactive test case, with several published computations available [2, 20, 16, 8] for turbulent reactive flows. However, because of the lack of concrete knowledge regarding the effect of turbulence on combustion, in this work the flow was computed assuming fully laminar flow. This will produce different results than those obtained using a turbulence model, but a grid convergence study may still be pursued to determine the robustness of the numerical model. In addition, most of the researchers who attempted this computation used grids leading to solutions that were severely underresolved, both in the boundary layer region and in the reaction zone. Thus, any results that were obtained must be viewed in this light.

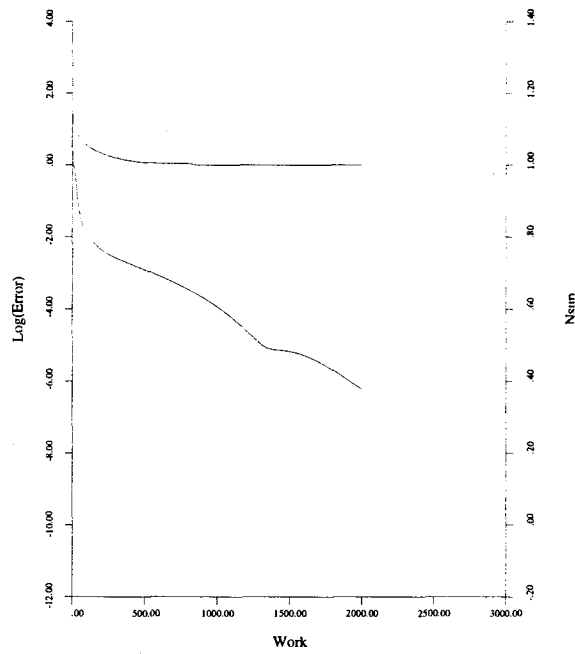


Figure 18: Multigrid convergence history: $M = 2.10$ hydrogen/air 6.34° viscous ramp. Grid size: 128×96 .

This flow was computed using Westbrook's nine species, seventeen reaction hydrogen-air mechanism because other researchers have used this model for this test case. This is a very challenging flow because of the myriad of physical phenomena that must be resolved accurately. The formation of the boundary layer must be captured well, without unnecessary dissipation, so that the displacement thickness is correct. The conduction of heat must also be accurate so that the effects of viscous dissipation deep in the boundary layer are felt correctly in the sections of the boundary layer far from the wall. Proper resolution of the interaction of the shock and boundary layer and the oscillation free capture of the shock are essential, as is the correct modeling of species diffusion. The free stream temperature is not high enough to initiate a reaction, but the combination of high temperature in the boundary layer, diffusion of radicals in the direction normal to the wall and the oblique shock cause a reaction front to form past the shock in the ramp region. Any inaccuracy will cause the location of the reaction front to be incorrect.

An assiduous grid convergence study was undertaken for this flow. Three grids were used to simulate this flow and to determine the robustness of the algorithm. All three grids had cells clustered near the wall to properly capture the laminar boundary layer, with approximately 32 cells within the boundary layer. In addition, cells were clustered near the start of the ramp, where shock-boundary layer interaction may lead to interesting phenomena. We

would expect any artificial diffusion of mass, momentum and energy to decrease as the grid resolution increases. In addition, the modeling of convective and diffusive transport is second order accurate and thus, the accuracy of the physical transport should increase as the grid spacing becomes smaller. Figures 19, 20 and 21 show the temperature in the flow field for three grids of size 64×96 , 64×108 and 128×156 , with the first number of cells along the wall and the second number of cells normal to the wall. As was expected, the formation

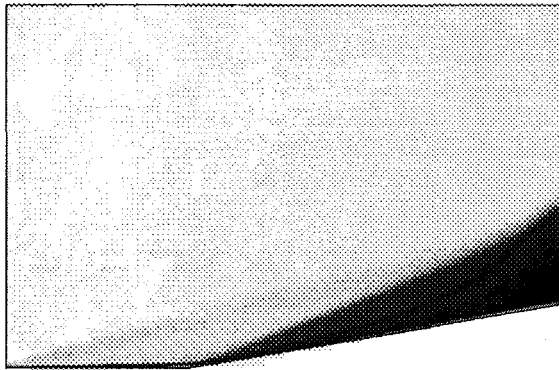


Figure 19: Temperature: $M = 4.0$ hydrogen/air 10° viscous ramp, 64×96 grid. Temperature range: 1200–3500 K.

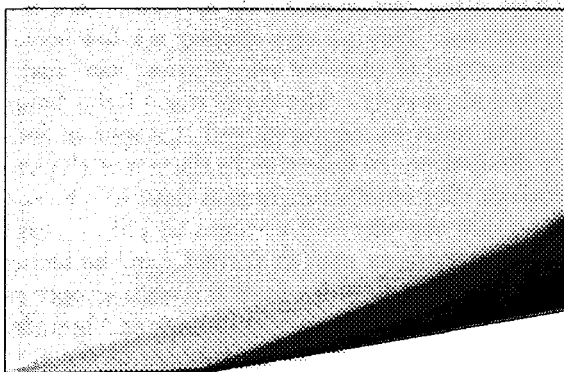


Figure 20: Temperature: $M = 4.0$ hydrogen/air 10° viscous ramp, 64×108 grid. Temperature range: 1200–3500 K.

of the boundary layer and the attendant viscous dissipation raises the temperature near the wall which causes various radical species to form. This leads to the formation of some water vapor very near the wall before the shock, but does not greatly affect the flowfield. One may also notice the formation of a weak oblique shock at the left edge of the domain due to the displacement thickness of the boundary layer. The interaction of the stronger oblique shock and the boundary layer at the ramp corner separates the boundary layer for a short distance and



Figure 21: Temperature: $M = 4.0$ hydrogen/air 10° viscous ramp, 128×156 grid. Temperature range: 1200–3500 K.

causes a small recirculation zone in that region. Beyond the oblique shock, the increased temperature and pressure lead to faster radical production and increased diffusion of those radicals and heat to the unreacted bulk flow behind the shock. The result is a reaction front that forms and gradually moves away from the wall. The reaction front may be seen in a different way by viewing the mass fraction of water in Figure 22 for the 128×156 grid. Comparing

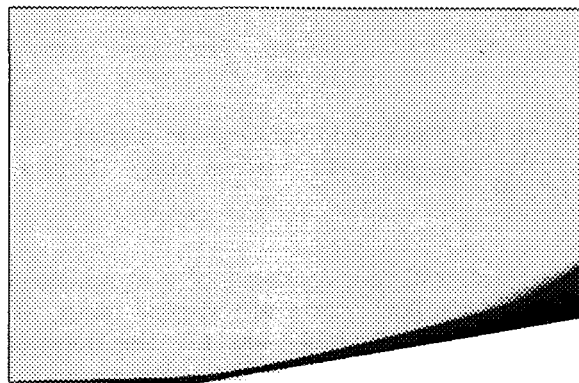


Figure 22: Water mass fraction: $M = 4.0$ hydrogen/air 10° viscous ramp, 128×156 grid. Mass fraction range: 0.00–0.18.

the results of the three grid simulations yields interesting insights into the resolution needed for this flow. The third grid (128×156) has twice the resolution of the first grid (64×96) in both the normal and streamwise directions outside of the boundary layer. The result is that the reaction front is unphysically diffused on the coarser grid (due to inadequate resolution of the reaction zone, artificial diffusion of radical species and energy and inadequate resolution for diffusive transport) and is captured quite well on the finest grid. The curvature of the reaction front at the right edge of the domain may be an actual physical phenomenon or it may be a numerical ar-

tifacit. If it is a spurious numerical phenomenon, it is probably due to one of two causes. First, it may be that the supersonic extrapolation boundary conditions at the outflow plane are contaminating the solution. Second, the numerical dissipation may be causing unphysical diffusion of radical species and heat. However, it is unlikely, given the resolution of this grid in that particular area, that the artificial dissipation is the cause. Thus, in order to test the accuracy of the boundary condition, an additional simulation was performed in which the outflow plane of the simulation domain was moved approximately 0.9 cm downstream. The computational size of this additional simulation was also 128×156 cells, with 32 cells again within the boundary layer.

The results of this extended domain simulation are presented in Figures 23 through 25. The flow field temperature is depicted in Figure 23, where the solid line within the simulation domain indicates the former outflow plane location. Comparing this figure to Figure 21, one can see that the temperature in the smaller domain and the extended domain match exceptionally well in the original computational region. Water mass fraction is shown in Figure 24, while pressure may be viewed in Figure 25. The extension of the domain makes it evidently clear that the curvature of the reaction front observed in Figures 21 and 22 is indeed a true physical phenomenon. In addition, the simulation on the extended domain indicates that the use of the supersonic extrapolation boundary conditions at the outflow plane does not compromise the accuracy of the solution in the region of the boundary. In this flow, radicals and heat in the boundary layer diffuse outward normal to the wall and eventually, along with the increased temperature and pressure behind the oblique shock, cause the reaction to proceed in the inviscid region behind the oblique shock. This reaction front couples with the shock toward the outflow plane and changes the angle of the discontinuity in the flow due to the pressure and heat release behind the shock/reaction front.

Other researchers' previously published results for this flow were calculated on grids with half as many cells in the normal direction as the finest grid presented here. These simulations show a coupled shock reaction front located much closer to the ramp corner in which the shock curves away from the wall. While these other simulations were computed with turbulence models of varying complexity, it is probably the underresolution of the reaction area which leads to the greatest disparity between those results and those presented here. If the reaction area is underresolved and the numerical scheme is too dissipative, then a probable result would be for the reaction zone to move upstream to the shock position. This would be caused by unphysical diffusion of radical



Figure 23: Temperature for extended domain: $M = 4.0$ hydrogen/air 10° viscous ramp, 128×156 grid. Temperature range: 1200–3500 K. Solid line in the computational domain indicates original outflow boundary.

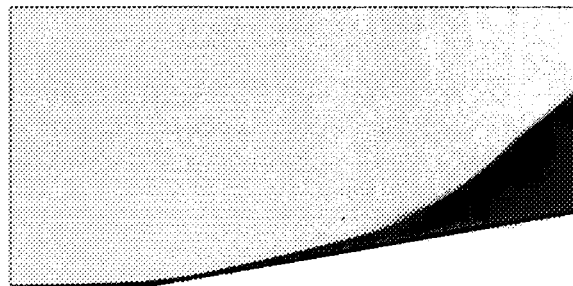


Figure 24: Water mass fraction for extended domain: $M = 4.0$ hydrogen/air 10° viscous ramp, 128×156 grid. Mass fraction range: 0.00–0.18.

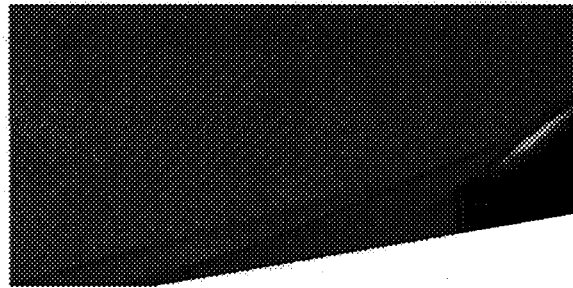


Figure 25: Normalized pressure for extended domain: $M = 4.0$ hydrogen/air 10° viscous ramp, 128×156 grid. Normalized pressure range: 0.00–6.00.

species and thermal energy upstream, allowing the reaction to commence earlier and thus move toward the shock. In fact, early simulations of this flow field with the current method using a very coarse grid were characterized by the reaction front moving upstream and away from the wall toward the shock location.

Conclusions

An accurate solver for the steady-state Euler and Navier-Stokes equations with chemical reactions has been developed, and preliminary results have been presented. The CUSP dissipation scheme yields accurate capture of shocks, reaction zones and reaction fronts for both inviscid axisymmetric and viscous two-dimensional test cases while the use of multigrid acceleration techniques leads to a significant decrease in computational time without sacrificing accuracy.

Acknowledgements

This work was funded by AFOSR-URI F49620-93-1-0427. The first author was supported in part by a Fannie and John Hertz Foundation/Princeton Research Center Fellowship.

References

- [1] T. R. A. Bussing and E. M. Murman. Finite-volume method for the calculation of compressible chemically reacting flows. *AIAA Journal*, 26(9):1070–1078, September 1988.
- [2] T. Chitsomboon, A. Kumar, and S. N. Tiwari. Numerical study of finite-rate supersonic combustion using parabolized equations. *AIAA paper 87-0088*, AIAA 25th Aerospace Sciences Meeting and Exhibit, Reno, NV, January 1987.
- [3] J. S. Evans and C. J. Schexnayder. Influence of chemical kinetics and unmixedness on burning in supersonic hydrogen flames. *AIAA Journal*, 18(2):180–193, February 1980.
- [4] J. Fielding. An experimental study of supersonic laminar reacting boundary layers. Master's thesis, Princeton University, Department of Mechanical and Aerospace Engineering, January 1997.
- [5] C. J. Jachimowski. An analytical study of the hydrogen-air reactions mechanism with application to scramjet combustion. NASA TP 2791, 1988.
- [6] A. Jameson. Analysis and design of numerical schemes for gas dynamics 1, artificial diffusion, upwind biasing, limiters and their effect on multigrid convergence. *Int. J. of Comp. Fluid Dyn.*, 4:171–218, 1995.
- [7] A. Jameson. Analysis and design of numerical schemes for gas dynamics 2, artificial diffusion and discrete shock structure. *Int. J. of Comp. Fluid Dyn.*, 5:1–38, 1995.
- [8] Y. Ju. Lower-upper scheme for chemically reacting flow with finite rate chemistry. *AIAA Journal*, 33(8):1418–14256, August 1995.
- [9] T. J. Kim, R. A. Yetter, and F. L. Dryer. New results on moist CO oxidation: High pressure, high temperature experiments and comprehensive kinetic modeling. Twenty-Fifth Symposium (International) on Combustion, The Combustion Institute, 1994.
- [10] H. F. Lehr. Experiments on shock-induced combustion. *Astronautica Acta*, 17:589–596, 1972.
- [11] L. Martinelli. *Calculation of Viscous Flows with a Multigrid Method*. PhD thesis, Princeton University, Department of Mechanical & Aerospace Engineering, October 1987.
- [12] L. Martinelli and A. Jameson. Validation of a multigrid method for the Reynolds Averaged equations. *AIAA paper 88-0414*, AIAA 26th Aerospace Sciences Meeting, Reno, NV, January 1988.
- [13] A. Matuso, K. Fujii, and T. Fujiwara. Flow features of shock-induced combustion around projectile traveling at hypervelocities. *AIAA Journal*, 33(6):1056–1063, June 1995.
- [14] S. G. Sheffer. *Parallel Computation of Supersonic Reactive Flows with Detailed Chemistry Including Viscous and Species Diffusion Effects*. PhD thesis, Princeton University, Department of Mechanical and Aerospace Engineering, June 1997.
- [15] S. G. Sheffer, A. Jameson, and L. Martinelli. Parallel computation of supersonic reactive flows with detailed chemistry. *AIAA paper 97-0899*, AIAA 35th Aerospace Sciences Meeting, Reno, NV, January 6–9 1997.
- [16] J. S. Shuen and S. Yoon. Numerical study of chemically reacting flows using a lower–upper symmetric successive overrelaxation scheme. *AIAA Journal*, 27(12):1752–1760, December 1989.

- [17] S. Tatsumi, L. Martinelli, and A. Jameson. Design, implementation, and validation of flux limited schemes for the solution of the compressible Navier-Stokes equations. *AIAA paper 94-0647*, AIAA 32nd Aerospace Sciences Meeting, Reno, NV, January 1994.
- [18] C. K. Westbrook. Hydrogen oxidation kinetics in gaseous detonations. *Combustion Science and Technology*, 29:67–81, 1982.
- [19] G. J. Wilson and R. W. MacCormack. Modeling supersonic combustion using a fully implicit numerical method. *AIAA Journal*, 30(4):1008–1015, April 1992.
- [20] H. C. Yee and J. L. Shinn. Semi-implicit and fully implicit shock-capturing methods for nonequilibrium flows. *AIAA Journal*, 27(3):299–307, March 1989.
- [21] R. Yetter and J. Fielding. Princeton University, 1996. Private communication.
- [22] R. A. Yetter, F. L. Dryer, and D. M. Golden. Pressure effects on the kinetics of high speed chemically reacting flows. ICASE/NASA Series, New York, 1992. Springer-Verlag. In Major Research Topics in Combustion.
- [23] S. Yungster, S. Eberhardt, and A. P. Bruckner. Numerical simulation of hypervelocity projectiles in detonable gases. *AIAA Journal*, 29(2):187–199, February 1991.